

Ligand and Solvent Effects on the Structural and Optical Properties of $\text{Au}_{13}\text{L}_8^{3+}$ Clusters: a Density Functional Theory Study

Edna S. Machado,[Ⓛ]^a Nailton M. Rodrigues,^a Marcus V. A. Prado,^b José D. L. Dutra,^a
Nivan B. da Costa Júnior^a and Viviane C. Felicíssimo^{*a}

^aDepartamento de Química, Universidade Federal de Sergipe,
Av. Marechal Rondon, s/n, Jardim Rosa Elze, 49100-000 São Cristóvão-SE, Brazil

^bDepartamento de Física, Universidade Federal de Sergipe,
Av. Marechal Rondon, s/n, Jardim Rosa Elze, 49100-000 São Cristóvão-SE, Brazil

Density functional theory (DFT) calculations have been performed to develop a systematic structural analysis of $\text{Au}_{13}\text{L}_8^{3+}$, where $\text{L} = \text{SCH}_3, \text{SeCH}_3, \text{SCH}_2\text{OCH}_3$ and $\text{S}(\text{CH}_2)_2\text{NH}_2$, in order to examine the influence of different ligands. Binding energy calculations indicate that the gold core is more stabilized by the ligand in the following sequence $\text{S}(\text{CH}_2)_2\text{NH}_2 > \text{SCH}_2\text{OCH}_3 > \text{SeCH}_3 > \text{SCH}_3$. Natural bond orbital (NBO) analysis describes the interaction between the gold and the ligands, showing that the strongest electron donation occurs from a lone pair orbital on the sulfur and selenium atoms to the antibonding acceptor $\sigma^*(\text{Au}-\text{S})$ and $\sigma^*(\text{Au}-\text{Se})$ orbitals, respectively. The NBO analysis allowed to understand the origin of enhanced stability of the $[\text{Au}_{13}(\text{S}(\text{CH}_2)_2\text{NH}_2)_8]^{3+}$. Time-dependent DFT (TDDFT) calculations have been performed to simulate the optical absorption spectra of $\text{Au}_{13}\text{L}_8^{3+}$ in gas phase and under the effect of solvents with different polarities. The absorption spectrum of $[\text{Au}_{13}(\text{S}(\text{CH}_2)_2\text{NH}_2)_8]^{3+}$ shows a spectral profile that differs considerably from the others in gas phase and which is strongly affected by the solvent.

Keywords: gold clusters, DFT calculations, optical spectrum, solvent effect

Introduction

The physical chemical properties of gold clusters and their dependence with atomic arrangement (shape) and size (number of atoms) have driven the interest of researchers for some decades.¹⁻³ Among the properties of the gold clusters, the magnetic,⁴ catalytic,⁵⁻⁷ electrochemical,^{8,9} optical¹⁰⁻¹² and structural¹³ ones have been intensively studied, which lead to promising applications in nanoelectronics, chemical sensing, catalysis, biomedicine, etc.¹⁴⁻¹⁶ Many of these properties are affected by the strong relativistic effect present on gold atoms.^{17,18} This feature explains the trend of gold atoms to generate clusters of different sizes, in contrast with other analogous metals like silver and copper.¹⁹ In general, small Au_n clusters ($n = 2-10$) are usually planar,^{20,21} while transition structures from 2D to 3D are formed at $n = 11-13$ ^{22,23} and, for $n > 13$, the 3D structures are predominant.^{24,25}

Among Au clusters, the Au_{13} has been focus of particular interest for being the smallest geometrically stable shell-

closed structure (“magic number”).²⁶ Besides that, this cluster exists in a variety of structures, a fact that is explored in many studies.²⁷⁻³⁰ The most popular one shows icosahedral (I_h) symmetry, since it is present as subunits of larger clusters, like Au_{25} ³¹ and Au_{38} .³² On the other hand, the structures of smaller clusters such as Au_9 and Au_{11} are observed as fragments of icosahedral Au_{13} .^{27,33} Nonetheless, other Au_{13} isomers have been studied: cuboctahedron, decahedron, planar and flake.^{28,30,34} Ding *et al.*,³⁴ in a theoretical study, investigated through density functional theory (DFT) calculations the energetic stability of some of these geometrical structures. The results indicate that the planar structure of Au_{13} is the most stable in energy. However, for the thiolate-protected $\text{Au}_{13}(\text{SCH}_3)_{12}$, the icosahedral geometry is the one with the lowest energy, followed by the planar, cuboctahedron and flake.

Although the icosahedral structure is perhaps the most frequently studied geometry for metallic nanoclusters,²⁹ we consider the octahedral (O_h) symmetry of Au_{13} in this study. This can be justified in order to keep the face-centered-cubic (fcc) structure of the bulk gold that, by a spherical cut, originates the Au_{13} as being the smallest

*e-mail: felicissimo@ufs.br

gold cluster with O_h symmetry. An extra motivation comes from the experimental work of Negishi and Tsukuda.³⁵ They prepared the Au_{13} with O_h symmetry in which the eight (111) facets of the gold cluster are fully passivated by eight *meso*-2,3-dimercaptosuccinic acid (DMSA) ligands. They also predicted a structural model for the $Au_{13}(DMSA)_8$ cluster where the sulfur atom of the DMSA ligand is bonded to the three gold atoms of each (111) facet of the cuboctahedral Au_{13} .

Beyond the geometrical structure of the gold core, another important factor exhibited by the clusters is the influence of different ligands. It has been pointed that the ligand influence interferes in many properties of the cluster.^{8,9,36,37} Aikens,³⁶ in 2010, investigated the changes in the absorption spectra of $Au_{25}(SPhX)_{18}^-$ induced by different ligands, $X = H, F, Cl, Br, CH_3$ and OCH_3 . She observed that the chemical nature of ligand slightly affects the optical absorption spectra, being the $X = OCH_3$ that most affects among the other ligands. In 2012, Jung *et al.*⁸ reported through DFT/PW91 calculations the influence of different thiolate ligands in the electrochemical and thermodynamic stability of gold nanoclusters: $Au_{25}(SR)_{18}^-$, $Au_{38}(SR)_{24}$ and $Au_{102}(SR)_{44}$, where $R(\text{aliphatic}) = CH_3, C_6H_{13}$ and CH_2CH_2Ph , and $R(\text{aromatic}) = Ph, PhF$ and $PhCOOH$. It was concluded that open-chain ligands presented a higher electrochemical and thermodynamic stability than the aromatic thiols, and the SCH_2CH_2Ph provides the highest stability among them. On the experimental point of view, Guo and Murray⁹ analyzed the ligand effect through the redox potential of $Au_{38}(SPhX)_{24}$ clusters (in which $X = NO_2, Br, H, CH_3, OCH_3$). The results showed that the electron acceptor ligands favor energetically the reduction instead of oxidation. A later paper, published in 2015 by Chen *et al.*,³⁷ presented a strategy to obtain gold nanoclusters with varied sizes, $Au_{40}(MBT)_{24}$, $Au_{104}(MBT)_{41}$ and $Au_{130}(MBT)_{50}$, and using as stabilizer the isomers *ortho*-, *meta*-, *para*-methylbenzenethiol (MBT), respectively. They concluded that the nanocluster size decreases as the position of methyl group in MBT ligand goes from *para* to *ortho*, which is caused by steric hindrance of the group CH_3 with the interfacial Au-S bond.

Besides the ligand influence, it has been reported that the solvent effect also affects the structural, electronic and optical properties of gold clusters.³⁸⁻⁴³ From the structural point of view, Jiang *et al.*³⁹ showed that solvents with higher polarity tend to form thiolate clusters with smaller sizes due to hydrogen bonding interactions. Recently, Thanthirige *et al.*⁴³ observed the characteristics of the absorption spectra of bi-icosahedral Au_{25} clusters in ethanol and toluene, under different temperatures. At room temperature the results were similar for both solvents.

But, at 78 K, it was observed a different behavior in the absorption spectrum profile between the solvents: when the toluene had been substituted by ethanol, there was a red-shift of the lowest energy band, and also new peaks appear in the 400 nm region.

Therefore, this work reports a systematic theoretical investigation, at DFT level, about the influence of different ligands and the solvent effect on the structural and optical properties of cuboctahedral Au_{13}^{3+} cluster capped with one ligand on each face (111). The choice of the triply charged metal cluster is motivated by the article of Nobusada⁴⁴ who explains that the monolayer-protected metal clusters (MPCs) are usually synthesized in solvents, where there are counterpart negative ions, such as halogens, in such an environment. Thus, compounds in ionic forms, such as $Au_{13}L_8^{k+} + k Cl^-$, are also present together with neutral compounds $Au_{13}L_8$. Furthermore, to avoid performing DFT calculations taking into account the high-spin state (i.e., the quartet state) of the neutral $Au_{13}L_8$, the $Au_{13}L_8^{3+}$ was chosen. Therefore, we investigated the system $Au_{13}L_8^{3+}$, where $L = SCH_3, SeCH_3, SCH_2OCH_3$ and $S(CH_2)_2NH_2$. It was analyzed solvents with different polarities (water (H_2O) > ethanol (C_2H_5OH) > dichloromethane (CH_2Cl_2) > tetrahydrofuran (C_4H_8O) > toluene (C_7H_8) > hexane (C_6H_{14})).

Methodology

All calculations have been performed on the framework of DFT⁴⁵ as implemented in the ORCA program package.⁴⁶ The electronic structure of the excited states and related optical properties of all molecular systems were calculated with time dependent density functional theory (TDDFT) methodology.⁴⁷ The Becke's three-parameter exchange functional combined with Lee, Yang and Parr (LYP) correlation functional, known as B3LYP,⁴⁸⁻⁵⁰ was employed in all calculations carried out here. The 6-311++G(d,p) basis set⁵¹ was used for the H, S, C, N, O and Se atoms, while for the gold atoms the Los Alamos effective-core potential (ECP) LANL2DZ basis set⁵² were applied. All geometries were fully optimized considering the $Au_{13}L_8^{3+}$ clusters in gas phase or under the effect of the solvents. The default convergence criteria were used in all geometry optimizations (energy change: $5.0 \times 10^{-6} E_h$, maximum gradient: $3.0 \times 10^{-4} E_h/\text{bohr}$, root-mean-square (RMS) gradient: $1.0 \times 10^{-4} E_h/\text{bohr}$, maximum displacement: $4.0 \times 10^{-3} \text{ bohr}$ and RMS displacement: $2.0 \times 10^{-3} \text{ bohr}$). The initial geometry used in the optimization calculations was built from the optimized structure of the cuboctahedral Au_{13}^{3+} in gas phase in which the pre-optimized ligand is added to each of the eight (111) facets of the gold cluster. Excitations to the lowest 50 states were evaluated for

the optical spectra. The absorption spectra were fit with a Gaussian function with a half width at half maximum (HWHM) of 0.13 eV. To improve computational speed of the excited states, the RIJCOSX⁵³ approximation was applied. The conductor-like polarizable continuum model (C-PCM)^{54,55} was used for the treatment of implicit solvation effects on the absorption spectra. Finally, the natural bond orbital (NBO) analysis⁵⁶ was employed to obtain the natural charges and the charge transfer between the metallic cluster and the ligands using the commercially available Gaussian09 software package.⁵⁷ The NBOs of several selected clusters were plotted using the GaussView program.⁵⁸

Results and Discussion

Structural properties-structure and stability

The optimized geometry of the $\text{Au}_{13}\text{L}_8^{3+}$, where $\text{L} = \text{SCH}_3, \text{SeCH}_3, \text{SCH}_2\text{OCH}_3$ and $\text{S}(\text{CH}_2)_2\text{NH}_2$, is presented in Figure 1 and the respective structural parameters are summarized in Table 1. The uncertainties in Table 1 are calculated as the standard deviation of the set of all chemically equivalent structural parameters in the cluster. The structures of $[\text{Au}_{13}(\text{SCH}_3)_8]^{3+}$ and $[\text{Au}_{13}(\text{SeCH}_3)_8]^{3+}$ are optimized within O_h molecular symmetry, while for the SCH_2OCH_3 and $\text{S}(\text{CH}_2)_2\text{NH}_2$ ligands, it is observed a light compression along one of the 4-fold axes reducing the cluster symmetry from O_h to D_{4h} .

Analyzing the results of $[\text{Au}_{13}(\text{SCH}_3)_8]^{3+}$ with the ones from its similar selenolate cluster, $[\text{Au}_{13}(\text{SeCH}_3)_8]^{3+}$, it can be noted some structural differences between them. The average length of the Au–Se bond is larger than the

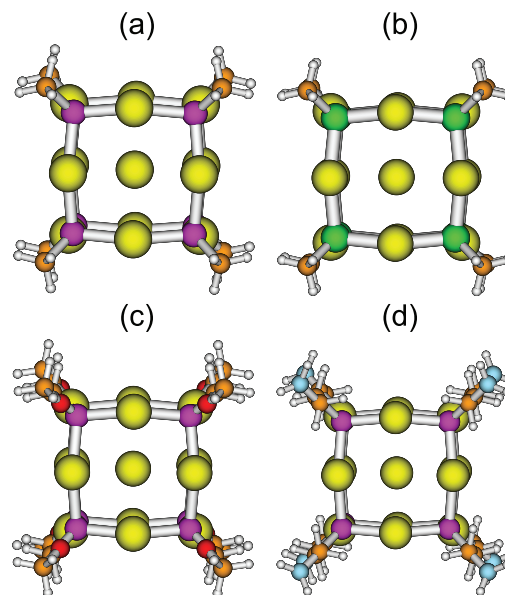


Figure 1. Optimized structures of (a) $[\text{Au}_{13}(\text{SCH}_3)_8]^{3+}$; (b) $[\text{Au}_{13}(\text{SeCH}_3)_8]^{3+}$; (c) $[\text{Au}_{13}(\text{SCH}_2\text{OCH}_3)_8]^{3+}$; (d) $[\text{Au}_{13}(\text{S}(\text{CH}_2)_2\text{NH}_2)_8]^{3+}$ in gas phase. Color labels: yellow: Au, pink: S, green: Se, orange: C, red: O, blue: N and white: H.

Au–S bond in the $[\text{Au}_{13}(\text{SCH}_3)_8]^{3+}$ cluster. This increase is attributed to the larger covalent radius of the Se atom ($r = 1.20 \text{ \AA}$) in contrast to the S atom ($r = 1.05 \text{ \AA}$). The same behavior is observed in the average distance of Se–C (1.987 \AA) and S–C (1.846 \AA) bonds. The substitution of the thiolate ligands SCH_3 by the selenolate SeCH_3 promotes an increase of the average distance between the central and surrounding gold atoms ($\text{Au}_c\text{--Au}_s$) and between two surrounding neighboring gold atoms ($\text{Au}_s\text{--Au}_s$). Thus, it is expected that this substitution affects not only the structural characteristics of the cluster, but also the electron density distribution and the molecular orbital energies.⁵⁹

Table 1. Structural parameters (bond lengths and bond angles) of the $\text{Au}_{13}\text{L}_8^{3+}$ clusters and their binding energies (E_b)

Parameter	$\text{Au}_{13}\text{L}_8^{3+}$			
	$\text{L} = \text{SCH}_3$	$\text{L} = \text{SeCH}_3$	$\text{L} = \text{SCH}_2\text{OCH}_3$	$\text{L} = \text{S}(\text{CH}_2)_2\text{NH}_2$
$r(\text{Au}_c\text{--Au}_s) / \text{\AA}$	3.642 ± 0.003	3.819 ± 0.002	3.636 ± 0.001	3.643 ± 0.000
$r(\text{Au}_s\text{--Au}_s) / \text{\AA}$	3.642 ± 0.001	3.819 ± 0.001	3.627 ± 0.000	3.625 ± 0.003
$r(\text{Au}_s\text{--S}) / \text{\AA}$	2.390 ± 0.000		2.385 ± 0.000	2.385 ± 0.000
$r(\text{Au}_s\text{--Se}) / \text{\AA}$		2.487 ± 0.000		
$r(\text{S--C}) / \text{\AA}$	1.846 ± 0.002		1.868 ± 0.000	1.865 ± 0.000
$r(\text{Se--C}) / \text{\AA}$		1.987 ± 0.000		
$\angle (\text{Au}_s\text{--S--Au}_s) / \text{degree}$	99.292 ± 0.031		98.973 ± 0.015	98.841 ± 0.001
$\angle (\text{Au}_s\text{--Se--Au}_s) / \text{degree}$		100.270 ± 0.034		
$\angle (\text{Au}_s\text{--S--C}_s) / \text{degree}$	118.391 ± 0.105		117.017 ± 0.075	119.235 ± 0.001
$\angle (\text{Au}_s\text{--Se--C}_s) / \text{degree}$		117.623 ± 0.048		
E_b / eV	–3.05	–3.10	–3.15	–3.20

Au_c : central gold atom; Au_s : surrounding gold atom.

Comparing the calculated geometrical parameters of the $[\text{Au}_{13}(\text{SCH}_3)_8]^{3+}$ with those from the other thiolate clusters, it can be observed that the substitution of the SCH_3 ligand by SCH_2OCH_3 or $\text{S}(\text{CH}_2)_2\text{NH}_2$ changes slightly the structural parameters of thiolate-protected gold clusters. This result is in agreement with the study of Weerawardene and Aikens,² who showed that the replacement of a large aromatic ligand (the 4-*tert*-butylbenzenethiol, TBBT) by a small aliphatic ligand (SCH_3) does not cause significant changes in the geometric parameters of $\text{Au}_{20}\text{R}_{16}$, $\text{R} = \text{CH}_3$ and TBBT.

In order to investigate the stabilization of the cuboctahedral Au_{13} clusters, the binding energies, E_b , in the following reaction were computed: $\text{Au}_{13}^{3+} + 8\text{L} \rightarrow \text{Au}_{13}\text{L}_8^{3+}$. These values are defined as $E_b = E_{\text{Au}_{13}\text{L}_8^{3+}} - (E_{\text{Au}_{13}^{3+}} + 8 \times E_{\text{L}})$ per L unit and they are shown in Table 1. Among all ligands studied in this work, the results clearly show that $\text{S}(\text{CH}_2)_2\text{NH}_2$ is the one which stabilizes the Au_{13}^{3+} cluster with more efficiency, followed by SCH_2OCH_3 , SeCH_3 , SCH_3 , respectively.

Structural properties-natural bond orbitals analysis

NBO analysis provides an accurate method for studying intra- and inter-molecular bonding and interaction among bonds, and also provides information about charge transfer or conjugative interaction in molecular systems.⁵⁶ In this study, the NBO method has been performed to quantify the donor-acceptor interactions between the gold cluster and the thiolate or selenolate ligands. Three types of donor-acceptor interactions were estimated through the second-order perturbation stabilization energy, $E(2)$, whose values are listed in Table 2, for all clusters investigated in this study. The NBO donor-acceptor overlaps of such interactions are presented in Figure 2, for the particular case of $[\text{Au}_{13}(\text{SCH}_3)_8]^{3+}$. The results analyzed below are

Table 2. Donor-acceptor natural bond orbital interactions in the $\text{Au}_{13}\text{L}_8^{3+}$ clusters and their second-order perturbation stabilization energies ($E(2)$)

$\text{Au}_{13}\text{L}_8^{3+}$	Charge transfer	$E(2) / (\text{kcal mol}^{-1})$
L = SCH_3	$n_{\text{S}} \rightarrow \sigma_{\text{Au}_i-\text{S}}^*$	49.36
	$\sigma_{\text{Au}_i-\text{S}} \rightarrow n_{\text{Au}_c}^*$	13.68
	$n_{\text{S}} \rightarrow n_{\text{Au}_i}^*$	9.56
L = SeCH_3	$n_{\text{Se}} \rightarrow \sigma_{\text{Au}_i-\text{Se}}^*$	54.78
	$\sigma_{\text{Au}_i-\text{Se}} \rightarrow n_{\text{Au}_c}^*$	20.19
	$n_{\text{Se}} \rightarrow n_{\text{Au}_i}^*$	13.85
L = SCH_2OCH_3	$n_{\text{S}} \rightarrow \sigma_{\text{Au}_i-\text{S}}^*$	67.95
	$\sigma_{\text{Au}_i-\text{S}} \rightarrow n_{\text{Au}_c}^*$	19.07
	$n_{\text{S}} \rightarrow n_{\text{Au}_i}^*$	10.66
L = $\text{S}(\text{CH}_2)_2\text{NH}_2$	$n_{\text{S}} \rightarrow \sigma_{\text{Au}_i-\text{S}}^*$	68.95
	$\sigma_{\text{Au}_i-\text{S}} \rightarrow n_{\text{Au}_c}^*$	20.28
	$n_{\text{S}} \rightarrow n_{\text{Au}_i}^*$	11.12

Au_c : central gold atom; Au_i : surrounding gold atom; n , n^* , σ and σ^* : refers, respectively, to the lone pair, empty lone pair, bonding and antibonding orbitals.

directed to the thiolate clusters, but a similar discussion can be considered to the selenolate cluster replacing sulfur atoms by selenium. From Table 2, one can see that two donor-acceptor interactions show that the 3p lone pair electrons of the sulfur atom (n_{S}) can transfer to either the 6p empty lone pair orbital of surrounding gold atom ($n_{\text{Au}_i}^*$) or to the antibonding σ^* orbital in the Au_i-S bond. However, the electron transfer from n_{S} to $\sigma_{\text{Au}_i-\text{S}}^*$ is more favored than to $n_{\text{Au}_i}^*$. This is demonstrated by the higher second-order perturbation stabilization energy $E(2)$ of $n_{\text{S}} \rightarrow \sigma_{\text{Au}_i-\text{S}}^*$. It is important to observe that the dominant donor-acceptor charge transfer interactions belong to adjacent subsystems. The third interaction presented in Table 2 indicates a donation of electrons from the bonding σ orbital in the

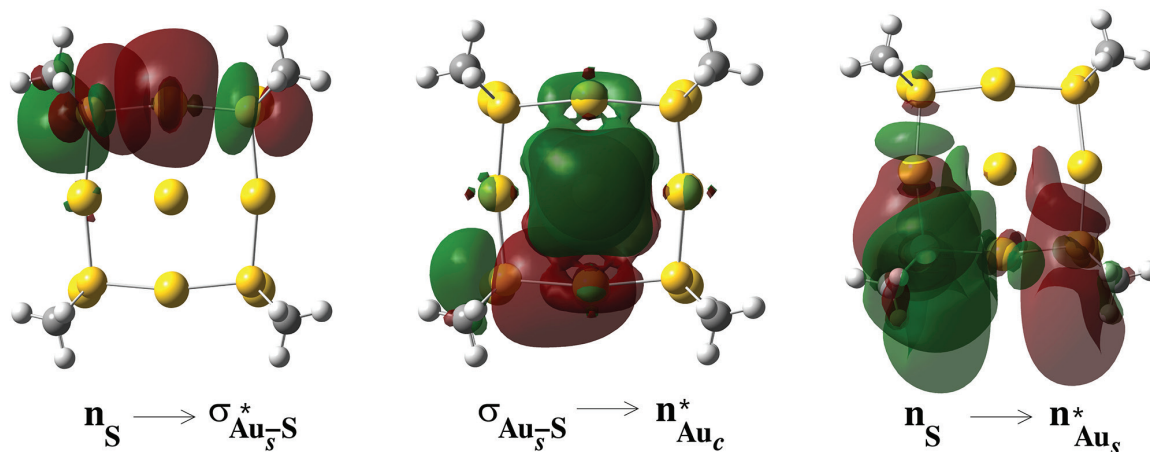


Figure 2. NBO orbitals associated with charge transfer analysis in $[\text{Au}_{13}(\text{SCH}_3)_8]^{3+}$.

$\text{Au}_s\text{-S}$ bond to the empty lone pair orbital of central gold atom ($n_{\text{Au}_c}^*$). The smaller second-order perturbation stabilization energy of such interaction demonstrates that the electron transfer from $\sigma_{\text{Au}_s\text{-S}}$ to $n_{\text{Au}_c}^*$ is less favored than $n_s \rightarrow \sigma_{\text{Au}_s\text{-S}}^*$.

Comparing the $E(2)$ values of the dominant donor-acceptor charge transfer interaction, $n_s \rightarrow \sigma_{\text{Au}_s\text{-S}}^*$, for the different clusters in Table 2, it is observed the same trend as binding energies: $[\text{Au}_{13}(\text{S}(\text{CH}_2)_2\text{NH}_2)_8]^{3+} > [\text{Au}_{13}(\text{SCH}_2\text{OCH}_3)_8]^{3+} > [\text{Au}_{13}(\text{SeCH}_3)_8]^{3+} > [\text{Au}_{13}(\text{SCH}_3)_8]^{3+}$. This result demonstrates that the ligand containing the amine group presents an enhanced capacity to stabilize the Au_{13}^{3+} cluster.

Among the thiolate clusters, the $[\text{Au}_{13}(\text{S}(\text{CH}_2)_2\text{NH}_2)_8]^{3+}$ and $[\text{Au}_{13}(\text{SCH}_2\text{OCH}_3)_8]^{3+}$ show the largest second-order perturbation stabilization energy $E(2)$ of 67.95 and 68.95 kcal mol^{-1} , respectively. Such values are higher than that of 49.36 kcal mol^{-1} in $[\text{Au}_{13}(\text{SCH}_3)_8]^{3+}$. This result is consistent with the shorter S–Au distance for the thiolate clusters containing the amine and ether groups, as one can see in Table 1.

Optical properties-ligand effects

In order to evaluate the effect of different ligands on the optical properties, we have performed TDDFT calculations to obtain the optical spectrum of $\text{Au}_{13}\text{L}_8^{3+}$, $\text{L} = \text{SCH}_3$, SeCH_3 , SCH_2OCH_3 and $\text{S}(\text{CH}_2)_2\text{NH}_2$. Although the $[\text{Au}_{13}(\text{SCH}_2\text{OCH}_3)_8]^{3+}$ and $[\text{Au}_{13}(\text{S}(\text{CH}_2)_2\text{NH}_2)_8]^{3+}$ present

a D_{4h} symmetry due to a light compression along one of the 4-fold axes, their *quasi*-degenerate molecular orbitals will be grouped according to the corresponding in the O_h symmetry: $a_{2u} + e_u \rightarrow t_{1u}$, $b_{2g} + e_g \rightarrow t_{2g}$ and $b_{1g} + a_{1g} \rightarrow e_g$. This will allow a standard interpretation for the spectral profile of the four clusters investigated in this study.

Firstly, the optical absorption spectrum of $[\text{Au}_{13}(\text{SCH}_3)_8]^{3+}$ is compared with its similar selenolate cluster, $[\text{Au}_{13}(\text{SeCH}_3)_8]^{3+}$. Thus, for these two systems, the calculated optical spectrum and the energy diagram of Kohn-Sham molecular orbitals (MO) with their respective atomic orbital (AO) contributions are shown in Figures 3A and 3B.

As one can see in Figures 3A and 3B, the absorption spectra of both systems show three feature peaks assigned as b, c and d. The transition from the highest occupied molecular orbital (HOMO) to the lowest unoccupied molecular orbital (LUMO), which is a forbidden $a_{1g} \rightarrow a_{1g}$ transition, is designed as peak a and it occurs at 2.04 eV for $[\text{Au}_{13}(\text{SCH}_3)_8]^{3+}$ and 1.87 eV for $[\text{Au}_{13}(\text{SeCH}_3)_8]^{3+}$. The HOMO-LUMO gap value decreases from $[\text{Au}_{13}(\text{SCH}_3)_8]^{3+}$ to $[\text{Au}_{13}(\text{SeCH}_3)_8]^{3+}$, which correlates with a red-shift of the absorption spectrum. Atomic orbital composition analyses reveal that the HOMO is composed almost exclusively from the one central Au(6s) atomic orbital, while the LUMO presents a preferential contribution from the surrounding Au(6s) and also from S(3s) or Se(4s) atomic orbitals, as it can be seen in their respective diagrams (Figures 3A and 3B). The Au(6s) contribution in HOMO and LUMO orbitals

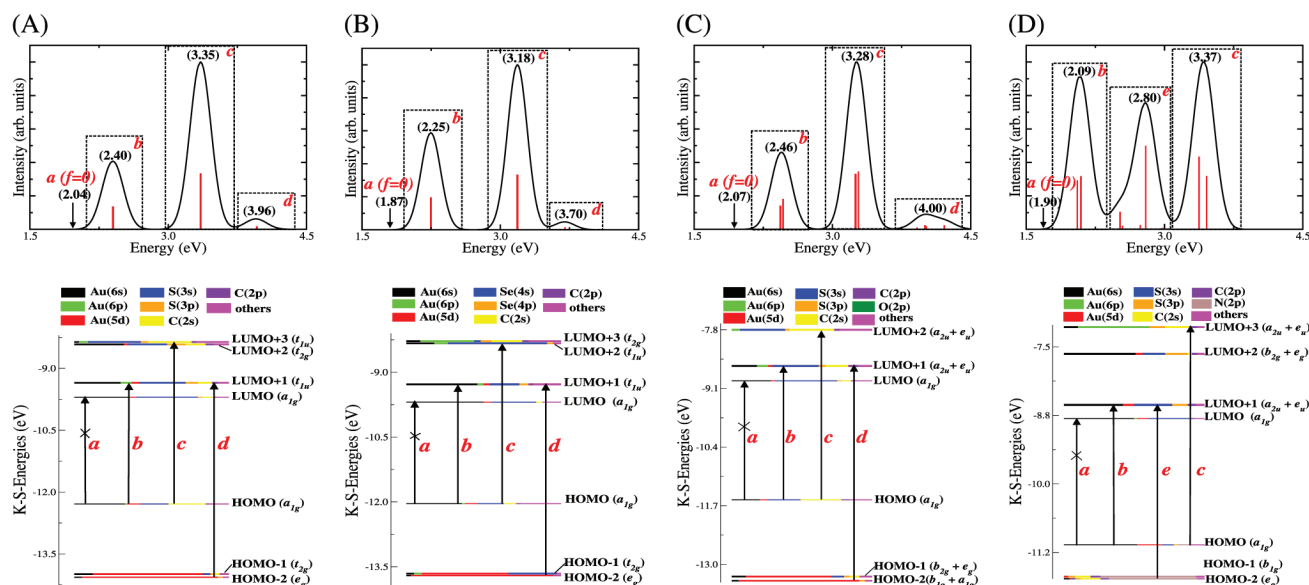


Figure 3. Theoretical absorption spectrum and the respective Kohn-Sham (KS) orbital level diagram of (A) $[\text{Au}_{13}(\text{SCH}_3)_8]^{3+}$; (B) $[\text{Au}_{13}(\text{SeCH}_3)_8]^{3+}$; (C) $[\text{Au}_{13}(\text{SCH}_2\text{OCH}_3)_8]^{3+}$ and (D) $[\text{Au}_{13}(\text{S}(\text{CH}_2)_2\text{NH}_2)_8]^{3+}$ clusters. Each KS orbital is drawn to indicate the relative contributions (line length with color labels) of the atomic orbitals. The orbital symmetry is indicated within O_h point group for (A) and (B) and within D_{4h} point group for (C) and (D). The *quasi*-degenerate KS orbitals in D_{4h} symmetry are grouped according to the O_h correlation table: $a_{2u} + e_u \rightarrow t_{1u}$, $b_{2g} + e_g \rightarrow t_{2g}$ and $b_{1g} + a_{1g} \rightarrow e_g$. The energy values of each peak are specified in the absorption spectra.

increases from thiolate to selenolate (33.0 and 34.1% in $[\text{Au}_{13}(\text{SCH}_3)_8]^{3+}$ and 36.0 and 50.3% in $[\text{Au}_{13}(\text{SeCH}_3)_8]^{3+}$).

The medium intensity peak assigned as b refers to the electronic transition from HOMO to the triply degenerate LUMO+1 and it is located at 2.40 and 2.25 eV for the thiolate and selenolate systems, respectively. The LUMO+1 is mostly composed from the surrounding Au unoccupied 6s and 6p orbitals. Thus, the HOMO \rightarrow LUMO+1 excitation induces electric charge transfer from the central gold atom to the surrounding ones.

A strong peak, indicated by c in both spectra of $[\text{Au}_{13}(\text{SCH}_3)_8]^{3+}$ and $[\text{Au}_{13}(\text{SeCH}_3)_8]^{3+}$ occurs, respectively, at 3.35 eV (oscillator strength, $f = 0.155$) and 3.18 eV ($f = 0.140$). Thus, the red-shift of 0.17 eV to the c peak keeps the same magnitude that is observed for the other peaks assigned in Figures 3A and 3B. The reason for this is that the replacement of the sulfur by the selenium atoms promotes, in general, a regular energy destabilization of the whole set of molecular orbitals, being more pronounced for the occupied (0.32 eV) than for the unoccupied orbitals (0.08 eV). Among the

unoccupied molecular orbitals, the LUMO+2 shows a more considerable energy destabilization (0.15 eV) causing a reordering of this orbital with LUMO+3 which is very close in energy. Thus, the c peak in $[\text{Au}_{13}(\text{SCH}_3)_8]^{3+}$ and $[\text{Au}_{13}(\text{SeCH}_3)_8]^{3+}$ refers to the electronic transition from HOMO to LUMO+3 and LUMO+2, respectively. The LUMO+3 orbital of the thiolate cluster and its equivalent LUMO+2 orbital of selenolate cluster have a majoritarian composition of the S and Se atomic orbitals, respectively, as seen in Figures 4a and 4b. Therefore, the c peak is attributed to the electronic transition which induces electric charge transfer from the central metal to the ligands. The analysis of the relative intensities of b, c and d peaks in the spectrum of Figures 3A and 3B reveals that such a charge transfer from the central metal to the ligands is responsible for the high intensity of c peak.

The highest energy feature absorption peak but with low intensity, assigned as d in Figures 3A and 3B, are located at 3.96 eV ($f = 0.008$) and 3.70 eV ($f = 0.005$), respectively. This peak is attributed to the electronic transition HOMO-2 \rightarrow LUMO+1. The doubly degenerate

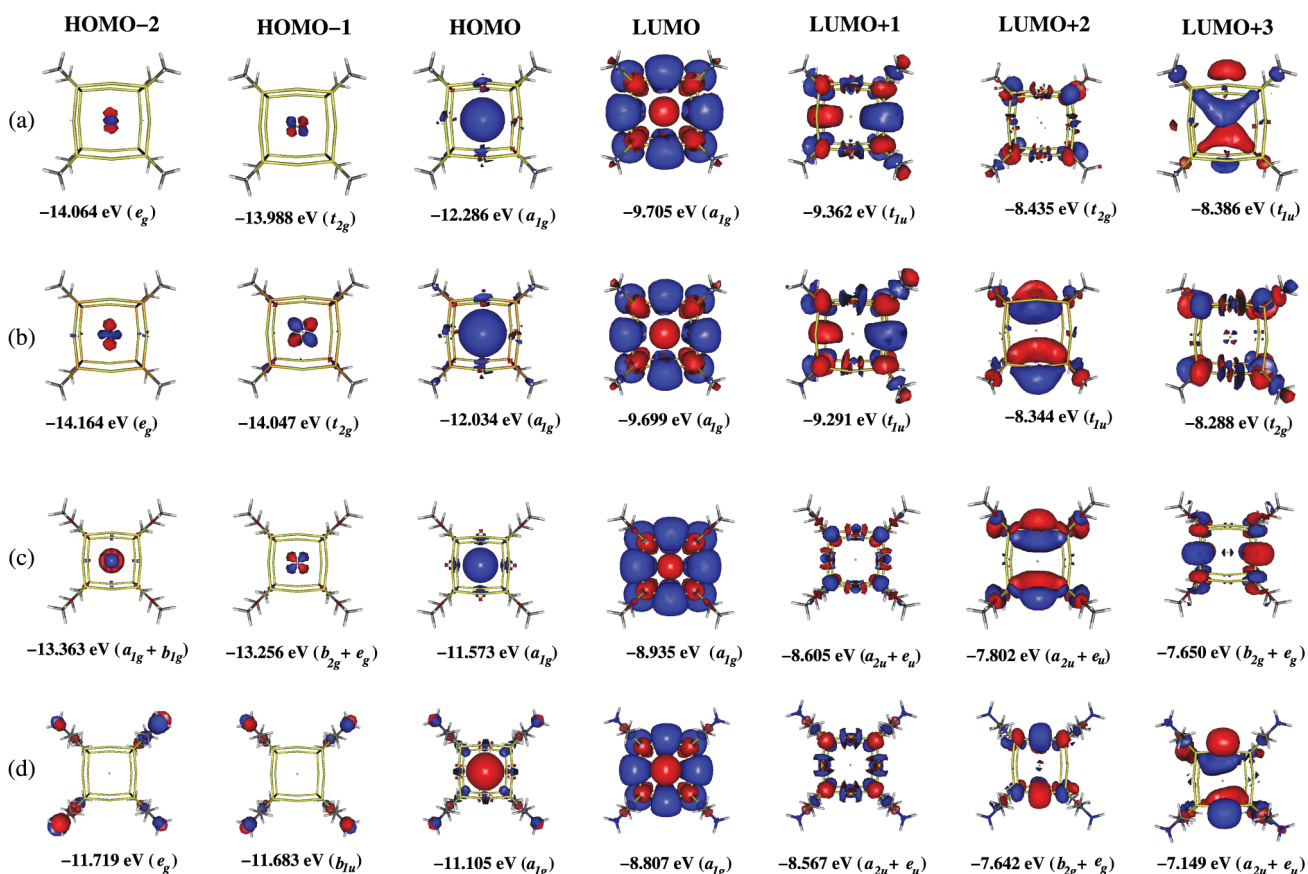


Figure 4. Molecular orbitals with the respective energies and symmetries of (a) $[\text{Au}_{13}(\text{SCH}_3)_8]^{3+}$; (b) $[\text{Au}_{13}(\text{SeCH}_3)_8]^{3+}$; (c) $[\text{Au}_{13}(\text{SCH}_2\text{OCH}_3)_8]^{3+}$; (d) $[\text{Au}_{13}\text{S}(\text{CH}_2)_2\text{NH}_2)_8]^{3+}$ clusters. The orbital symmetry is indicated within O_h point group for (a) and (b) and within D_{4h} point group for (c) and (d). The *quasi*-degenerate KS orbitals in D_{4h} symmetry are grouped according to the O_h correlation table: $a_{2u} + e_u \rightarrow t_{1u}$, $b_{2g} + e_g \rightarrow t_{2g}$ and $b_{1g} + a_{1g} \rightarrow e_g$. An average energy is indicated for the *quasi*-degenerate KS orbitals in D_{4h} symmetry.

HOMO-2 is composed mainly by the central Au(5d) atomic orbitals. Thus, the electronic transition related to the d peak corresponds to an electric charge redistribution from the central metal to the surrounding ones, as it was also observed for the d peak.

A similar analysis, as it was done above for the optical absorption spectra of thiolate and selenolate clusters, is expected for the spectrum of the thiolate cluster that contains the ether functional group, i.e., $[\text{Au}_{13}(\text{SCH}_2\text{OCH}_3)_8]^{3+}$. Its absorption spectrum and MO energy diagram are shown in Figure 3C. Three peaks assigned as b, c and d are observed in such spectrum and they occur at 2.46, 3.28 and 4.00 eV, respectively. Similar to the $[\text{Au}_{13}(\text{SeCH}_3)_8]^{3+}$ spectrum, the b and c peaks are also attributed to the electronic transitions HOMO \rightarrow LUMO+1 and HOMO \rightarrow LUMO+2, respectively. The three orbitals involved in these transitions also present a closely related composition of the AO's as those discussed above for the $[\text{Au}_{13}(\text{SeCH}_3)_8]^{3+}$ cluster.

A slight difference between the absorption spectra of the $[\text{Au}_{13}(\text{SCH}_3)_8]^{3+}$ and $[\text{Au}_{13}(\text{SCH}_2\text{OCH}_3)_8]^{3+}$ is noticed for the weak peak d. The d peak in the spectrum of the thiolate cluster containing the ether group has a contribution of both electronic transitions: HOMO-2 \rightarrow LUMO+1 and HOMO-3 \rightarrow LUMO. The extra contribution of the electronic transition HOMO-3 \rightarrow LUMO originates a subtle asymmetry in the band structure. The HOMO-3 orbital is composed almost exclusively from the ligand orbitals, that is, C(2s), O(2p) and H(1s), as seen in the energy diagram of Figure 3C. Thus, while the electronic transition HOMO-2 \rightarrow LUMO+1 induces an electric charge transfer from the central Au to the surrounding ones, the HOMO-3 \rightarrow LUMO is concerned to an electric charge redistribution from the ligands to the surrounding metals.

The optical absorption spectrum of $[\text{Au}_{13}(\text{S}(\text{CH}_2)_2\text{NH}_2)_8]^{3+}$ and the respective orbital energy diagram are presented in Figure 3D. Three absorption peaks b, e and c are located, respectively, at 2.09, 2.80 and 3.37 eV. Compared with the previous spectra discussed above, the b peak is similarly attributed to the electronic transition HOMO \rightarrow LUMO+1 and it also occurs at the lowest energy position. The c peak, regarding to the electronic transition HOMO \rightarrow LUMO+3, keeps with the largest oscillator strength but it appears with the highest energy position while the d peak is not observed in the spectrum of the cluster containing the amine group. However, a new peak assigned as e lies in the energy position between the peaks b and c. The e peak is attributed mainly to the electronic transition HOMO-2 \rightarrow LUMO+1. The HOMO-1 and HOMO-2 show a distinct composition from those verified for the other systems, being mostly composed from the N(2p) atomic orbitals. For the $[\text{Au}_{13}(\text{SCH}_3)_8]^{3+}$, $[\text{Au}_{13}(\text{SeCH}_3)_8]^{3+}$

and $[\text{Au}_{13}(\text{SCH}_2\text{OCH}_3)_8]^{3+}$, there is an average energy gap of 1.66 eV between the HOMO (central Au(6s)) and HOMO-1 (central Au(5d)). For the $[\text{Au}_{13}(\text{S}(\text{CH}_2)_2\text{NH}_2)_8]^{3+}$, due to the energy proximity between the valence orbitals of the isolated fragments (Au_{13}^{3+} and $\text{S}(\text{CH}_2)_2\text{NH}_2$), the orbitals composed strictly from the ligands containing the amine group appear between the orbitals with atomic character of the central gold, Au(6s) and Au(5d). Thus, the HOMO-2 \rightarrow LUMO+1 transition is related to an electric charge transfer from the amine group to the metals. A more significant contribution of the ligands in the composition of HOMO, HOMO-1 and HOMO-2 of $[\text{Au}_{13}(\text{S}(\text{CH}_2)_2\text{NH}_2)_8]^{3+}$ enhances the relative intensity of b and e peaks in relation to the c peak.

Optical properties-solvent effects

The effect of solvation on the optical absorption spectra of $\text{Au}_3\text{L}_8^{3+}$, L = SCH₃, SeCH₃, SCH₂OCH₃ and S(CH₂)₂NH₂ was taken into account using the C-PCM implicit solvation model. The absorption spectra of the clusters in solvents of different polarities are shown in Figure 5.

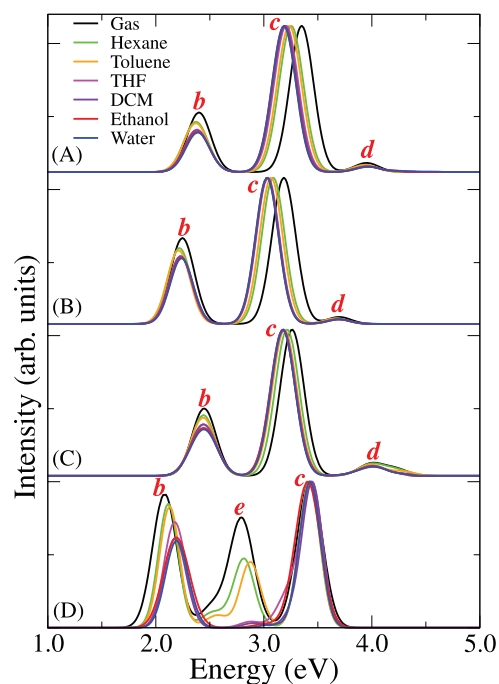


Figure 5. Optical absorption spectra in gas phase and under the effect of different solvents (A) $[\text{Au}_{13}(\text{SCH}_3)_8]^{3+}$; (B) $[\text{Au}_{13}(\text{SeCH}_3)_8]^{3+}$; (C) $[\text{Au}_{13}(\text{SCH}_2\text{OCH}_3)_8]^{3+}$; (D) $[\text{Au}_{13}(\text{S}(\text{CH}_2)_2\text{NH}_2)_8]^{3+}$ clusters.

As one can see in Figures 5A, 5B and 5C, the evolution of the spectra when the solvent polarity is increased show a similar trend for the clusters: $[\text{Au}_{13}(\text{SCH}_3)_8]^{3+}$, $[\text{Au}_{13}(\text{SeCH}_3)_8]^{3+}$ and $[\text{Au}_{13}(\text{SCH}_2\text{OCH}_3)_8]^{3+}$. The solvent effect is more pronounced for the c peak for which is

observed a red-shift of 0.16 eV for $[\text{Au}_{13}(\text{SCH}_3)_8]^{3+}$ and $[\text{Au}_{13}(\text{SeCH}_3)_8]^{3+}$ and 0.08 eV for $[\text{Au}_{13}(\text{SCH}_2\text{OCH}_3)_8]^{3+}$, as the solvent polarity is increased from gas phase to water. This result may be explained by considering that the electronic transition corresponding to c peak comprises the LUMO+3 (for $[\text{Au}_{13}(\text{SCH}_3)_8]^{3+}$) or its equivalent LUMO+2 (for $[\text{Au}_{13}(\text{SeCH}_3)_8]^{3+}$ and $[\text{Au}_{13}(\text{SCH}_2\text{OCH}_3)_8]^{3+}$), which presents a composition with the most significant contribution from the ligands which would be greatly affected by the solvent. The red-shift of c peak can be rationalized as a result of the LUMO+3 or LUMO+2 orbital energy being less destabilized than the HOMO energy by the more polar solvent field, reducing the energy difference between these orbitals. As the solvent polarity increases, going from gas phase to water, and using the MO energies of the ground electronic states, it is observed that the increase in energy of such unoccupied orbitals are 6.87 eV for $[\text{Au}_{13}(\text{SCH}_3)_8]^{3+}$, 6.69 eV for $[\text{Au}_{13}(\text{SeCH}_3)_8]^{3+}$ and 5.46 eV for $[\text{Au}_{13}(\text{SCH}_2\text{OCH}_3)_8]^{3+}$, while the increase in energy of HOMO for these three clusters are 7.04, 6.80 and 6.21 eV, respectively.

A distinct result is observed in the optical spectrum of $[\text{Au}_{13}(\text{S}(\text{CH}_2)_2\text{NH}_2)_8]^{3+}$ when the solvent effect is included, see Figure 5D. For this system, the solvent effect promotes a blue-shift of b and e peaks with increasing the solvent polarity. The b peak undergoes a blue-shift of 0.17 eV going from the $[\text{Au}_{13}(\text{S}(\text{CH}_2)_2\text{NH}_2)_8]^{3+}$ in gas phase to water, while for the e peak this shift is of 0.60 eV. This pronounced blue-shift of e peak results in its overlapping with c peak for higher solvent polarity. The electronic transitions regarding to the b and e peaks are, respectively, HOMO \rightarrow LUMO+1 and HOMO-2 \rightarrow LUMO+1. Thus, as the solvent polarity increases, increases also the energy difference between the orbitals involved in such electronic transitions caused by a progressive destabilization of the HOMO-2, HOMO and LUMO+1 energies, being more pronounced for the latter. The increase in energy of the HOMO-2, HOMO and LUMO+1, calculated from the MO energies of the ground electronic states, are 5.18, 5.83 and 5.96 eV, respectively, going from the $[\text{Au}_{13}(\text{S}(\text{CH}_2)_2\text{NH}_2)_8]^{3+}$ in gas phase to under the effect of water.

For the cluster containing the amine group it is observed that due to its significant contribution from the ligands, the unoccupied orbital LUMO+1 would be greatly affected by the solvent. Contrary to what was observed for the previous clusters, the solvent does not promote a significative shift of the c peak in the optical spectrum of $[\text{Au}_{13}(\text{S}(\text{CH}_2)_2\text{NH}_2)_8]^{3+}$. The c peaks corresponds to the HOMO \rightarrow LUMO+3 electronic transition. As the solvent polarity increases from gas phase to water, the HOMO and LUMO+3 energies undergo a progressive and

closer destabilization of 5.83 and 5.90 eV, respectively, keeping almost unchanged the energy difference between these orbitals. Due to this, the solvent does not affect significantly the position of c peak.

Conclusions

In this study, we employed density functional theory to investigate the effect of different ligands on the structural and optical properties of Au_{13}L_8 , with $\text{L} = \text{SCH}_3$, SeCH_3 , SCH_2OCH_3 and $\text{S}(\text{CH}_2)_2\text{NH}_2$. Firstly, we showed that the geometric parameters of the thiolate clusters are affected slightly with the variation of the ligand, while a more pronounced change is observed comparing the thiolate and selenolate clusters. The average of binding energies for the four clusters considered in this study has the order of $E_{\text{b}[\text{Au}_{13}(\text{S}(\text{CH}_2)_2\text{NH}_2)_8]^{3+}} (-3.20 \text{ eV}) > E_{\text{b}[\text{Au}_{13}(\text{SCH}_2\text{OCH}_3)_8]^{3+}} (-3.15 \text{ eV}) > E_{\text{b}[\text{Au}_{13}(\text{SeCH}_3)_8]^{3+}} (-3.10 \text{ eV}) > E_{\text{b}[\text{Au}_{13}(\text{SCH}_3)_8]^{3+}} (-3.05 \text{ eV})$. The NBO analysis show that the second-order perturbation stabilization energy, $E(2)$, of the dominant donor-acceptor charge transfer interaction, $n_s \rightarrow \sigma_{\text{Au}_i-\text{S}}$, presents the same trend as binding energies: $E(2)_{[\text{Au}_{13}(\text{S}(\text{CH}_2)_2\text{NH}_2)_8]^{3+}} (68.95 \text{ kcal mol}^{-1}) > E(2)_{[\text{Au}_{13}(\text{SCH}_2\text{OCH}_3)_8]^{3+}} (67.95 \text{ kcal mol}^{-1}) > E(2)_{[\text{Au}_{13}(\text{SeCH}_3)_8]^{3+}} (54.78 \text{ kcal mol}^{-1}) > E_{\text{b}[\text{Au}_{13}(\text{SCH}_3)_8]^{3+}} (49.36 \text{ kcal mol}^{-1})$. Both results demonstrate that the ligand containing the amine group shows an enhanced capacity to stabilize the Au_{13}^{3+} cluster. The optical absorption spectra have been simulated for the $\text{Au}_{13}\text{L}_8^{3+}$ in gas phase and under the effect of solvents with different polarities. The absorption spectra of $[\text{Au}_{13}(\text{SCH}_3)_8]^{3+}$, $[\text{Au}_{13}(\text{SeCH}_3)_8]^{3+}$ and $[\text{Au}_{13}(\text{SCH}_2\text{OCH}_3)_8]^{3+}$ show a similar profile, where the c peak, which is more affected by the solvent, presents a more pronounced red-shift as the solvent polarity increases. The optical spectrum of $[\text{Au}_{13}(\text{S}(\text{CH}_2)_2\text{NH}_2)_8]^{3+}$ shows a spectral profile that differs considerably from the others in gas phase where an extra peak, designed by e, is observed. The absorption spectrum of the cluster containing the amine group is strongly affected by the solvent, where a progressive blue-shift is observed for b and e peaks with the increase of the solvent polarity.

Acknowledgments

This work was supported by the Brazilian agencies Fundação de Apoio à Pesquisa e à Inovação Tecnológica do Estado de Sergipe (FAPITEC/SE) and Coordenação de Aperfeiçoamento de Pessoal de Nível Superior (CAPES). We thank Prof Ricardo Luiz Longo of Universidade Federal de Pernambuco (UFPE) for providing the use of Gaussian09 and GaussView programs. The computing for this project

was performed on the Laboratório de Computação de Alto Desempenho of UFS (LCAD-UFS).

References

1. Maity, P.; Xie, S.; Yamauchi, M.; Tsukuda, T.; *Nanoscale* **2012**, *4*, 4027.
2. Weerawardene, K. L. D. M.; Aikens, C. M.; *J. Phys. Chem. C* **2016**, *120*, 8354.
3. Jin, R.; *Nanoscale* **2015**, *7*, 1549.
4. Zhu, M.; Aikens, C. M.; Hendrich, M. P.; Gupta, R.; Qian, H.; Schatz, G. C.; Jin, R.; *J. Am. Chem. Soc.* **2009**, *131*, 2490.
5. Cunningham, D. A. H.; Vogel, W.; Kageyama, H.; Tsubota, S.; Haruta, M.; *J. Catal.* **1998**, *177*, 1.
6. Liu, Y.; Tsunoyama, H.; Akita, T.; Xie, S.; Tsukuda, T.; *ACS Catal.* **2011**, *1*, 2.
7. Yamazoe, S.; Koyasu, K.; Tsukuda, T.; *Acc. Chem. Res.* **2014**, *47*, 816.
8. Jung, J.; Kang, S.; Han, Y.-K.; *Nanoscale* **2012**, *4*, 4206.
9. Guo, R.; Murray, R. W.; *J. Am. Chem. Soc.* **2005**, *127*, 12140.
10. Aikens, C. M.; *J. Phys. Chem. C* **2008**, *112*, 19797.
11. Xie, J.; Zheng, Y.; Ying, J. Y.; *J. Am. Chem. Soc.* **2009**, *131*, 888.
12. Goel, S.; Velizhanin, K. A.; Piryatinski, A.; Ivanov, S. A.; Tretiak, S.; *J. Phys. Chem. C* **2012**, *116*, 3242.
13. Yan, L.; Cheng, L.; Yang, J.; *J. Phys. Chem. C* **2015**, *119*, 23274.
14. Yang, X.; Yang, M.; Pang, B.; Vara, M.; Xia, Y.; *Chem. Rev.* **2015**, *115*, 10410.
15. Wu, Z.; Wang, M.; Yang, J.; Zheng, X.; Cai, W.; Meng, G.; Qian, H.; Wang, H.; Jin, R.; *Small* **2012**, *8*, 2028.
16. Lin, C.-A. J.; Yang, T.-Y.; Lee, C.-H.; Huang, S. H.; Sperling, R. A.; Zanella, M.; Li, J. K.; Shen, J.-L.; Wang, H.-H.; Yeh, H.-I.; Parak, W. J.; Chang, W. H.; *ACS Nano* **2009**, *3*, 395.
17. Wang, L.-S.; *Phys. Chem. Chem. Phys.* **2010**, *12*, 8694.
18. Gorin, D. J.; Toste, F. D.; *Nanoscale* **2007**, *446*, 395.
19. Pykkö, P.; *Angew. Chem., Int. Ed.* **2004**, *43*, 4412.
20. De, H. S.; Krishnamurthy, S.; Mishra, D.; Pal, S.; *J. Phys. Chem. C* **2011**, *115*, 17278.
21. Olson, R. M.; Varganov, S.; Gordon, M. S.; Metiu, H.; Chretien, S.; Piecuch, P.; Kowalski, K.; Kucharski, S. A.; Musial, M.; *J. Am. Chem. Soc.* **2005**, *127*, 1049.
22. Spivey, K.; Williams, J. I.; Wang, L.; *Chem. Phys. Lett.* **2006**, *432*, 163.
23. Gruber, M.; Heimel, G.; Romaner, L.; Brédas, J.-L.; Zojer, E.; *Phys. Rev. B* **2008**, *77*, 165411.
24. Bulusu, S.; Zeng, X. C.; *J. Chem. Phys.* **2006**, *125*, 154303.
25. Gao, Y.; Shao, N.; Pei, Y.; Chen, Z.; Zeng, X. C.; *ACS Nano* **2011**, *5*, 7818.
26. Mingos, D. M. P. In *Gold Clusters, Colloids and Nanoparticles I*; Mingos, D. M. P., ed.; Springer International Publishing: Cham, 2014, p. 1-47.
27. Shichibu, Y.; Suzuki, K.; Konishi, K.; *Nanoscale* **2012**, *4*, 4125.
28. Pundlik, S. S.; Kalyanaraman, K.; Waghmare, U. V.; *J. Phys. Chem. C* **2011**, *115*, 3809.
29. Jin, R.; Zeng, C.; Zhou, M.; Chen, Y.; *Chem. Rev.* **2016**, *116*, 10346.
30. Shafai, G.; Hong, S.; Bertino, M.; Rahman, T. S.; *J. Phys. Chem. C* **2009**, *113*, 12072.
31. Heaven, M. W.; Dass, A.; White, P. S.; Holt, K. M.; Murray, R. W.; *J. Am. Chem. Soc.* **2008**, *130*, 3754.
32. Qian, H.; Eckenhoff, W. T.; Zhu, Y.; Pintauer, T.; Jin, R.; *J. Am. Chem. Soc.* **2010**, *132*, 8280.
33. Mingos, D. M. P.; *J. Cluster Sci.* **1992**, *3*, 397.
34. Ding, W.; Huang, C.; Guan, L.; Liu, X.; Luo, Z.; Li, W.; *Chem. Phys. Lett.* **2017**, *676*, 18.
35. Negishi, Y.; Tsukuda, T.; *J. Am. Chem. Soc.* **2003**, *125*, 4046.
36. Aikens, C. M.; *J. Phys. Chem. Lett.* **2010**, *1*, 2594.
37. Chen, Y.; Zeng, C.; Kauffman, D. R.; Jin, R.; *Nano Lett.* **2015**, *15*, 3603.
38. Dufour, F.; Fresch, B.; Durupthy, O.; Chaneac, C.; Remacle, F.; *J. Phys. Chem. C* **2014**, *118*, 4362.
39. Jiang, Y.; Huang, Y.; Cheng, H.; Liu, Q.; Xie, Z.; Yao, T.; Jiang, Z.; Huang, Y.; Bian, Q.; Pan, G.; Sun, Z.; Wei, S.; *J. Phys. Chem. C* **2014**, *118*, 714.
40. Rojas-Cervellera, V.; Rovira, C.; Akola, J.; *J. Phys. Chem. Lett.* **2015**, *6*, 3859.
41. Yao, H.; Tsubota, S.; *Chem. Phys.* **2017**, *493*, 149.
42. Zhou, M.; Lei, Z.; Guo, Q.; Wang, Q.-M.; Xia, A.; *J. Phys. Chem. C* **2015**, *119*, 14980.
43. Thanthirige, V. D.; Sinn, E.; Wiederrecht, G. P.; Ramakrishna, G.; *J. Phys. Chem. C* **2017**, *121*, 3539.
44. Nobusada, K.; *J. Phys. Chem. B* **2004**, *108*, 11904.
45. Parr, R. G. In *Horizons of Quantum Chemistry*; Fukui, K.; Pullman, A., eds.; Springer Netherlands: Dordrecht, 1980, p. 5-15.
46. Horcajada, P.; Chalati, T.; Serre, C.; Gillet, B.; Sebrie, C.; Baati, T.; Eubank, J. F.; Heurtaux, D.; Clayette, P.; Kreuz, C.; Chang, J. S.; Hwang, Y. K.; Marsaud, V.; Bories, P. N.; Cynober, L.; Gil, S.; Ferey, G.; Couvreur, P.; Gref, R.; *Nat. Mater.* **2010**, *9*, 172.
47. Runge, E.; Gross, E. K. U.; *Phys. Rev. Lett.* **1984**, *52*, 997.
48. Becke, A. D.; *Phys. Rev. A* **1988**, *38*, 3098.
49. Becke, A. D.; *J. Chem. Phys.* **1993**, *98*, 5648.
50. Lee, C.; Yang, W.; Parr, R. G.; *Phys. Rev. B* **1988**, *37*, 785.
51. Krishnan, R.; Binkley, J. S.; Seeger, R.; Pople, J. A.; *J. Chem. Phys.* **1980**, *72*, 650.
52. Hay, P. J.; Wadt, W. R.; *J. Chem. Phys.* **1985**, *82*, 270.
53. Kossmann, S.; Neese, F.; *J. Chem. Theory Comput.* **2010**, *6*, 2325.
54. Cossi, M.; Scalmani, G.; Rega, N.; Barone, V.; *J. Chem. Phys.* **2002**, *117*, 43.
55. Cossi, M.; Rega, N.; Scalmani, G.; Barone, V.; *J. Comput. Chem.* **2003**, *24*, 669.

56. Glendening, E. D.; Landis, C. R.; Weinhold, F.; *Wiley Interdiscip. Rev.: Comput. Mol. Sci.* **2011**, 2, DOI: <https://doi.org/10.1002/wcms.51>.
57. Frisch, M. J.; Trucks, G. W.; Schlegel, H. B.; Scuseria, G. E.; Robb, M. A.; Cheeseman, J. R.; Scalmani, G.; Barone, V.; Mennucci, B.; Petersson, G. A.; Nakatsuji, H.; Caricato, M.; Li, X.; Hratchian, H. P.; Izmaylov, A. F.; Bloino, J.; Zheng, G.; Sonnenberg, J. L.; Hada, M.; Ehara, M.; Toyota, K.; Fukuda, R.; Hasegawa, J.; Ishida, M.; Nakajima, T.; Honda, Y.; Kitao, O.; Nakai, H.; Vreven, T.; Montgomery Jr., J. A.; Peralta, J. E.; Ogliaro, F.; Bearpark, M. J.; Heyd, J.; Brothers, E. N.; Kudin, K. N.; Staroverov, V. N.; Kobayashi, R.; Normand, J.; Raghavachari, K.; Rendell, A. P.; Burant, J. C.; Iyengar, S. S.; Tomasi, J.; Cossi, M.; Rega, N.; Millam, N. J.; Klene, M.; Knox, J. E.; Cross, J. B.; Bakken, V.; Adamo, C.; Jaramillo, J.; Gomperts, R.; Stratmann, R. E.; Yazyev, O.; Austin, A. J.; Cammi, R.; Pomelli, C.; Ochterski, J. W.; Martin, R. L.; Morokuma, K.; Zakrzewski, V. G.; Voth, G. A.; Salvador, P.; Dannenberg, J. J.; Dapprich, S.; Daniels, A. D.; Farkas, Ö.; Foresman, J. B.; Ortiz, J. V.; Cioslowski, J.; Fox, D. J.; *Gaussian 09.B01*; Gaussian, Inc., Wallingford, USA, 2009.
58. Dennington, R.; Keith, T. A.; Millam, J. M.; *GaussView Version 6*; Semichem Inc., Shawnee Mission, 2016.
59. Song, Y.; Zhong, J.; Yang, S.; Wang, S.; Cao, T.; Zhang, J.; Li, P.; Hu, D.; Pei, Y.; Zhu, M.; *Nanoscale* **2014**, 6, 13977.

Submitted: October 1, 2018

Published online: March 12, 2019

